Polaron Size and Shape Effects on Oxygen Vacancy Interactions in Lanthanum Strontium Ferrite

Tridip Das, Jason D. Nicholas,* and Yue Qi*

Chemical Engineering & Materials Science Department, Michigan State University, 428 South Shaw Lane, 2527 Engineering Building, East Lansing, MI 48824, USA

Abstract

Both aliovalent doping and the charge state of multivalent lattice ions determine the oxygen non-stoichiometry (δ) of mixed ionic and electronic conductors (MIECs). Unfortunately, it has been challenging for both modeling and experiments to determine the multivalent ion charge states in MIECs. Here, the Fe charge state distribution was determined for various compositions and phases of the MIEC $La_{1-x}Sr_xFeO_{3-\delta}$ (LSF) using the spin-polarized density functional theory (DFT)-predicted magnetic moments on Fe. It was found that electron occupancy and crystal-field-splitting-induced differences between the Fe *3d*-orbitals of the square pyramidally coordinated, oxygen-vacancy-adjacent Fe atoms and the octahedrally-coordinated, oxygen-vacancy-distant-Fe atoms determined whether the excess electrons produced during oxygen vacancy formation remained localized at the first nearest neighbor Fe atoms (resulting in small oxygen polarons, as in $LaFeO_3$) or were distributed to the second-nearest-neighbor Fe atoms (resulting in large oxygen vacancy polarons, as in $SrFeO_3$). The progressively larger polaron size and anisotropic shape changes with increasing Sr resulted in increasing oxygen vacancy interactions, as indicated by an increase in the oxygen vacancy formation energy above a critical δ threshold. This was consistent with experimental results showing that Sr-rich LSF and highly oxygen deficient compositions are prone to oxygen-vacancy-ordering-induced phase transformations, while Sr-poor and oxygen-rich LSF compositions are not. Since oxygen vacancy induced phase transformations cause a decrease in the mobile oxygen vacancy site fraction (*X*), both δ and *X* were predicted as a function of temperature and oxygen partial pressure, for multiple LSF compositions and phases using a combined thermodynamics and DFT approach.

Keywords: Lanthanum Strontium Ferrite, Oxygen Vacancy, Polaron, Phase Transformation, Concentration

***Email:** jdn@msu.edu, yueqi@egr.msu.edu

1. INTRODUCTION

Due to their high electronic and oxygen ion conductivities, Mixed Ionic Electronic Conducting (MIEC) oxides are used for a variety of electrochemical devices including solid oxide fuel cells,[1–4] gas sensors,[5] gas separation membranes,[6] memristors,[7] etc. Unfortunately, the performance of these devices is often limited by poor oxygen transport within the MIEC.[8] For prototypical MIECs such as lanthanum strontium ferrite (LSF, $La_{1-x}Sr_xFeO_{3-\delta}$ ($0 \leq x \leq 1$), past studies have shown that the amount of aliovalent Sr doping, the charge distribution of the multivalent Fe cations, interactions between the oxygen vacancies, and the overall oxygen non-stoichiometry, δ, can impact the mobile oxygen vacancy site fraction, *X*, and hence the ionic conductivity.[8–11]

However, the mechanistic details explaining the complicated interplay between these factors has yet to be fully established.[2,3,8,12–14] It is well known that the low oxygen vacancy content of many "Sr-poor" LSF concentrations (such as the LSF end member $LaFeO_{3-\delta}$ (LFO) which has a large oxygen vacancy formation energy, ΔE_{vac}^{f}, of ~ 4 eV at 0 K)[10,15] can be increased through the extrinsic aliovalent Sr substitution of La via the reaction (in Kröger-Vink notation):

$$2SrO \rightarrow 2Sr'_{La} + 2O_O^x + V_O^{\bullet\bullet} \quad [1]$$

However, under many conditions, the extrinsic aliovalent Sr dopant level, x in $La_{1-x}Sr_xFeO_{3-\delta}$, does not independently determine δ because the mixed charge of Fe in $La_{1-x}Sr_xFeO_{3-\delta}$ (which varies from 3+ in $LaFeO_3$ to 4+ in $SrFeO_3$) can cause δ to vary from 0 to $\sim x/2$.[15,16] In LSF, this internal redox reaction can be written as:[15]

$$2Fe_{Fe}^{\bullet} + O_O^x \rightarrow \frac{1}{2}O_{2(g)} + V_O^{\bullet\bullet} + 2Fe_{Fe}^x \quad [2]$$

In addition, the overall oxygen non-stoichiometry, δ, is not always proportional to the mobile oxygen vacancy site fraction, *X*. For instance, the LSF end member $SrFeO_{3-\delta}$ (SFO) has a very low

$\Delta E_{vac}^{f} \approx 0.4$ eV and hence at room temperature it possesses a δ of 0.03, but the X is so low at high temperature that it is seldom used for SOFC applications.[17–19] This is because as δ increases, the average distance between the oxygen vacancies shrinks, and beyond a critical δ (or below a critical vacancy-to-vacancy distance) oxygen vacancy interactions lead to an increase in the oxygen vacancy formation energy,[20,21] and eventually oxygen vacancy interactions induce phase transformations that decrease X by rearranging oxygen vacancies into a non-mobile, orderly array.[17,18] This partitioning of δ between X and the number of non-mobile oxygen vacancies per formula unit structurally required to form the particular crystal structure, δ^0, is summarized by the equation:

$$\delta = \delta^0 + (3 - \delta^0)X \quad [3]$$

While many past studies have justified the LSF conductivity maximum occurring at intermediate LSF compositions as a compromise between doping and oxygen vacancy ordering,[15,22] a detailed understanding of the mechanistic reasons why some intermediate compositions and/or phases are better than others has yet to emerge.

MIEC oxygen vacancy ordering is often discussed in terms of oxygen vacancy polarons, which Landau[23] defined as the excess charge (generated here during the formation of a charge neutral oxygen vacancy) and the surrounding lattice strain field. Since the excess electrons generated during oxygen vacancy formation both screen the charge on their associated oxygen vacancy site and induce lattice distortions, they impact the formation of subsequent oxygen vacancies at high δ. While it is hard to exactly define polaron size and shape because the partial excess charges are distributed to both the Fe and O atoms around a missing lattice oxygen,[24,25] for simplicity, one can estimate the polaron size and shape based on the spatial deviations in transition metal charge states alone. For example, Castleton *et al.*,[25] defined the oxygen vacancy polaron in

ceria as the localized electrons on two Ce atoms adjacent to an oxygen vacancy site.[26] Our recent SFO study[19] also took this approach and found that the strong oxygen vacancy interactions in this LSF end member were due to a very large oxygen vacancy polaron size. Specifically, it was found that electron occupancy and crystal-field-splitting-induced differences between the 3d electron orbitals of the square pyramidally coordinated, oxygen-vacancy-adjacent Fe atoms and the octahedrally-coordinated, oxygen-vacancy-second-nearest-neighboring Fe atoms caused the two electrons left behind during oxygen vacancy formation in cubic SFO to spread to the second nearest neighbor Fe (instead of the Fe directly connected to the vacancy) resulting in extended lattice distortions that promoted strong oxygen vacancy interactions.[19] However, the distribution of the excess electrons generated by oxygen vacancy formation in $La_{1-x}Sr_xFeO_{3-\delta}$ has not been examined. Further, a detailed understanding of the relationship between the Fe charge state distribution associated with polaron and oxygen vacancy interactions in LSF has been missing from the literature. This is partially due to the difficulty in determining the actual Fe charge distribution within LSF, for both experimentalists and theorists.[10,15,16,27,28] For instance, while it is recognized that $La_{1-x}Sr_xFeO_{3-\delta}$ has a mixture of both Fe^{3+} and Fe^{4+} ions, it is still debated where Fe^{3+} or Fe^{4+} sits in vacancy-containing lattices.

Unfortunately, past attempts to understand the relationship between the Fe charge state distribution, the La:Sr ratio, and the oxygen vacancy interactions in LSF have been limited. For instance, Ritzmann *et al.,*[10] calculated that the oxygen vacancy formation energy, ΔE_{vac}^{f}, increased in $La_{0.75}Sr_{0.25}FeO_{3-\delta}$, decreased in $La_{0.5}Sr_{0.5}FeO_{3-\delta}$, and remained a constant in LFO, when δ increased from 1/32 to 1/8. However, their interesting δ-dependent oxygen vacancy formation energies did not contain an analysis of the oxygen vacancy interactions or the Fe oxidation states in LSF. Further, Mastrikov *et al.,*[29] showed that ΔE_{vac}^{f} increased with higher La:Sr ratio in LSF

(from SFO to $La_{0.5}Sr_{0.5}FeO_{3-\delta}$ (LSF55) to LFO) at a fixed $\delta = 1/8$. This increase of ΔE_{vac}^{f} with increasing La:Sr ratio was qualitatively related to the oxidation state on Fe but the reasons for the measured δ peak around a La:Sr ratio of 0.6:0.4 were not discussed. Furthermore, even though the experimental results of Dann *et al.*,[30] Patrakeev *et al.*,[16] and Fossdal *et al.*,[31] have confirmed that the $La_{1-x}Sr_xFeO_{3-\delta}$ crystal structure evolves from orthorhombic ($0 \leq x \leq 0.2$) to rhombohedral ($0.4 \leq x \leq 0.7$) to cubic ($0.8 \leq x \leq 1.0$) at room temperature, and Fossdal *et al.*[31] observed a rhombohedral to cubic second-order phase transition when rhombohedral LSF55 was heated from room temperature to 523±50 K (in air), these phase changes were not well captured in previous DFT-based oxygen vacancy calculations. For example, Ritzmann *et al.*[10] and Mastrikov *et al.*[29] used a cubic supercell for all LSF structures where *x* ranged from 1/32 to 1/8, even though experiments have shown that LSF is not cubic at those La:Sr ratios. Recently Taylor *et al.* used an orthorhombic supercell for LFO but unfortunately did not explore other La:Sr ratios.[32]

Therefore, the aim of the present study was to correctly establish the underlying mechanistic relationships between the La:Sr ratio, the Fe charge state, the oxygen vacancy polaron size and shape, δ and *X*. Here, three different LSF compositions, $LaFeO_{3-\delta}$ (LFO), $La_{0.5}Sr_{0.5}FeO_3$ (LSF55) and ($SrFeO_3$) SFO were studied. SFO and LFO represent the parent phases[31] of LSF and LSF55 was selected for its high oxygen ionic conductivity[16,22] and as a representative structure of the commonly used SOFC cathode material LSF64 ($La_{0.6}Sr_{0.4}FeO_{3-\delta}$).[3,15] The study objectives were achieved using a combined thermodynamics and DFT+*U* approach performed by first, appropriately selecting a suitable *U* parameter (as described in Sections 2.2. and 3.1a), second, using a magnetic moment interpreted charge calculation, instead of the traditional and in this case insensitive Bader charge analysis, to determine the Fe charge state (as described in Section 3.1b), third, validating the DFT simulations with known experimentally determined physical properties

(as described in Sections 3.1c and 3.2), fourth, calculating the effect of oxygen vacancy interactions on ΔE_{vac}^{f} (as described in Section 3.3), and fifth, using a previously-developed thermodynamic model[19] to predict *X* for various LSF compositions and phases under SOFC operating conditions.

2. COMPUTATIONAL DETAILS

2.1 DFT Calculation Details for $La_{1-x}Sr_xFeO_3$ (LSF) Structures

The plane wave based *ab initio* simulation package, VASP (Vienna *Ab initio* Simulation Package) was used for all the ground state (0 K, zero pressure) calculations. Projector-augmented-wave (PAW) potentials with valence configurations of $5s^25p^65d^16s^2$ for La, $4s^24p^65s^2$ for Sr, $3d^74s^1$ for Fe, and $2s^22p^4$ for O were used to describe the valence electrons. The generalized gradient approximation (GGA) functional along with Perdew, Burke, and Ernzerhof (PBE) parameters were used to describe the exchange-correlation potentials of the constituting elements. Fe was treated with the GGA+U method with a U_{eff} = 3. A detailed discussion of the Fe atom U parameter selection process is provided in Sections 2.2 and 3.1a. Spin-polarized calculations were performed and the magnetic moment on each Fe was calculated by spherical integration. The accuracy for the electronic calculations was within 1 μeV. A single point energy calculation was performed to test the convergence of the cut-off energy and *k*-points for each input lattice. It was concluded from the *k*-mesh calculations that a *k*-spacing of 0.2 $Å^{-1}$ was sufficient for the required accuracy of 1 meV/atom when the cutoff energy was set to 500 eV. Ionic relaxations were performed until the Hellmann-Feynman force on each atom reached the order of 10 meV/ Å.[33]

The ground state energy for all three oxygen-stoichiometric (i.e. δ = 0) LSF compositions was calculated with six different initial structures (three crystal structures, as shown in Fig 1, multiplied with two magnetic ordering arrangements), by allowing the cell shape and atom

positions to relax. Among these six input structures, the one with the minimum energy per formula unit was considered as the (ground state) crystal structure for that composition. The calculated crystal structures, lattice parameters, bond lengths, low-temperature magnetic ordering arrangements, and band gaps for stoichiometric SFO, LSF55, and LFO were benchmarked with experimental or computational studies whenever available in the literature.

2.2 Selection of U Parameter

DFT with a Hubbard-*U* approach (DFT+U)[34] was used to address the on-site electronic interactions of the *3d*-orbitals in the multivalent Fe atoms. This method has been shown to accurately predict the enthalpy of formation for oxides, the open circuit voltage in Li-ion batteries, phase diagrams, chemical reaction barriers, etc. for many transition-metal-containing materials.[8,35–37] In the DFT+U framework, spherically averaged Coulombic and exchange interactions for the electrons, denoted by U and J respectively, enter into DFT calculations as overhead terms.[38] Following the approach of Dudarev *et al.,*[34] these U and J parameters can be combined as $U_{eff} = U - J$, or used simply as a U parameter. The Hubbard-*U* parameter can be selected either directly employing *ab initio* methods like constrained-DFT[38,39] or based on empirically fitting experimental properties such as the band gap, magnetic moment, lattice parameters, bulk modulus, etc.[7,34,36,40,41] In some DFT+U studies, different transition metal charge states were treated with different U parameters. For example, Mosey *et al.,*[39] treated Fe^{2+} and Fe^{3+} with U_{eff} = 3.7 and 4.3 respectively, giving reasonable lattice parameter, magnetic moment, band gap and other physical property agreement for Fe_2O_3 and FeO. However, the energies calculated with different U parameters should not be compared (since the electrons are more localized with

increasing U), making it impossible to use that approach to perform comparative studies of different LSF phases containing mixed Fe oxidation states.

In the present study, because the local formal charge state on Fe was allowed to vary from 2+ ~ 4+ (due to the changing La/Sr ratio and the changing oxygen vacancy content), a single U parameter was required to treat all the multi-valent Fe atoms. GGA+U calculations were performed for (orthorhombic, FM) LFO and (cubic, FM) SFO with the U parameter over a range of 0.2 to 4.0 eV. The U-parameter was selected based on a careful comparison with the experimentally observed magnetic moments (as shown in Figure 2a) and lattice parameters (as shown in Figure 2b) of the LSF end members. The reason behind the selection of U to match both LFO and SFO was that the charge on Fe in LSF varies between 3+ and 4+, and the charge on Fe in LSF can be further interpreted as a linear mixing of 3+ and 4+ (as shown in Figure 3).[42]

2.3 Calculation of the Oxygen Vacancy Formation Energy (0 K) and Oxygen Vacancy Formation Free Energy (as a Function of Temperature and Oxygen Partial Pressure)

For the defect reaction given in Equation 2, the neutral oxygen vacancy formation energy, ΔE_{vac}^{f}, was calculated from the DFT+U predicted energy of a stoichiometric lattice (δ=0), $E_{perfect}^{DFT}$, and non-stoichiometric lattice, $E_{defective}^{DFT}$ (with one oxygen vacancy), using the relationship:[33]

$$\Delta E_{vac}^{f} = E_{defective}^{DFT} - E_{perfect}^{DFT} + \frac{1}{2}E_{O_2}^{DFT} \quad [4]$$

where, $E_{O_2}^{DFT}$ is the energy of an isolated oxygen molecule.[43] A detailed discussion of the computation of $E_{O_2}^{DFT}$ is available in Das *et al.*.[19] Here, ΔE_{vac}^{f} was calculated with different δ by varying the supercell size, mimicking a uniform vacancy distribution.

To facilitate direct comparison with experimentally measured δ values, the computed ΔE_{vac}^{f} was converted to an oxygen vacancy formation free energy, ΔG_{vac}^{f}, as a function of temperature (T) and oxygen partial pressure (p_{O_2}) using the relationship:[44,45]

$$\Delta G_{vac}^{f} = \Delta E_{vac}^{f} + \frac{1}{2}\left(\Delta \mu_{O_2}^{0}(T) + kTlnp_{O_2}\right) \quad [5]$$

where, $\Delta \mu_{O_2}^{0}(T)$ is the free energy of oxygen gas at a temperature T and standard state pressure (p_{O_2}= 1 bar), including the excess energy due to phonon vibration contributed by the lattice oxygen. The calculation of $\Delta \mu_{O_2}^{0}(T)$ was performed utilizing available thermodynamics data, as reported in Das *et al*.[19] Since ΔG_{vac}^{f} may increase with increasing LSF oxygen non-stoichiometry, a generalized equation to predict the oxygen vacancy site fraction, X as a function of temperature, oxygen partial pressure and vacancy concentration was utilized:

$$\frac{X}{1-X} = \exp\left(-\frac{\Delta G_{vac}^{f}(T,p,X)}{RT}\right) \quad [6]$$

Note, this equation can be used for both dilute and interacting vacancies. The oxygen vacancy site fractions were calculated by solving Equation 6.[19]

3. RESULTS AND DISCUSSIONS

3.1 Validation with Experiments

First, the calculation methods were tested for their ability to accurately predict the experimentally observed LSF crystal structures, lattice parameters, and low temperature Fe magnetic ordering arrangements. According to experiments, the representative LFO, SFO, and LSF55 compositions exhibit orthorhombic, cubic, and rhombohedral structures, respectively, at room temperature.[13,17,46] In addition to the different crystalline structures shown in Figure 1, they can also exhibit magnetic ordering, as indicated by Mössbauer results showing G-type Fe

antiferromagnetic (AFMG) ordering for $0 < x < 0.3$ and paramagnetic Fe ordering for $x > 0.4$, at room temperature.[47]

a) Calibration of the U Parameter Based on the Fe Magnetic Moment and Lattice Parameters of the LSF End Members

Figure 2a shows a comparison between the experimental and computed Fe magnetic moments with varying U-parameter (from 0.2 to 4) for LFO and SFO, represented by lines and solid dots, respectively. SFO showed a steady increase in the magnetic moment of Fe with increasing U parameter but the magnetic moment of Fe in LFO fluctuated (Figure 2a), possibly due to the existence of additional minima as a result of different possible electronic distributions.[48] The experimental magnetic moment for Fe in LFO was reported by Koehler *et al.*[49] as $\mu_{Fe^{3+}} = 4.6 \pm 0.2$ μ_B (Figure 2a, dashed line) and it is a widely acceptable value in the literature.[50–52] In contrast, difficulty in the experimental sample preparation of stoichiometric cubic SFO[53,54] has resulted in a large variability in the experimentally measured Fe magnetic moments in SFO.[54–56] Nevertheless, most of the experimental data indicates that Fe has a high spin state in SFO.[53,57–59] In a recent comprehensive study, Reehuis *et al.*[54] measured the magnetic moment on Fe in stoichiometric cubic SFO as $\mu_{Fe^{4+}} = 2.96$ μ_B (Figure 2a, dotted line) with neutron diffraction, at 2 K.

Figure 2b compares the computed lattice parameters of LFO and SFO with experimental results. Note, to allow a comparison of the computed and experimental lattice parameters in a single plot, all the LFO lattice parameters were divided by $\sqrt{2}$ before plotting in Figure 2b. As done previously for SFO,[19] based on a comparison of the computed versus experimental lattice parameters and magnetic moments for both LFO and SFO in Figure 2, a $U_{eff} = 3$ was selected.

With this value of U, the lattice parameters showed a maximum deviation of 1.75 % from their experimentally-measured room temperature values. The selection of U_{eff} = 3 also resulted in a reasonable agreement between the computed and experimentally measured magnetic moments. The computed magnetic moment was $\mu_{Fe^{3+}}$ = 4.23 μ_B for Fe^{3+} in LFO, and was $\mu_{Fe^{4+}}$ = 3.61 μ_B for the Fe^{4+} present in SFO, both of which were similar to the experimental values.[49,50,54] In some earlier computational studies with multivalent Fe atoms, the focus was on Fe^{3+} containing compounds, for which a U_{eff} = 4 [60] or 5.4 [61] was employed. However, only a few studies exist where Fe multi-valence states were treated with a single U parameter. For example, Muñoz-García *et al.,*[62] treated 2+, 3+, and 4+ charge states on Fe with U_{eff} = 4 and Ritzmann *et al.,*[10] used U_{eff} = 5.4, where the Fe charge state varied from 3+ to 3.5+. One consequence of using such a high U-parameter is that the vacancy formation energy might be underestimated.[19] For example, it was reported in our previous study that U_{eff} = 4 would lead to a lower oxygen vacancy formation energy in SFO, resulting in a ~200˚C difference in the temperature required to generate the oxygen non-stoichiometry observed in cubic $SrFeO_{3-\delta}$ in the air.[19] Thus, when Ritzmann *et al.,*[10] used U_{eff} = 5.4 in their calculations, the underestimated vacancy formation energy led to an unphysical (negative) oxygen vacancy formation free energy at 700ºC for LSF55. As will be shown in Section 3.1b and c, a U_{eff}=3 also gave the correct band gap and phases for various SFO compositions and phases.

b) Magnetic Moment Interpreted Charge versus Total Bader Charge

Bader charge analysis is a widely used and efficient method to define formal charge on atoms.[63,64] However, as shown in Table 1, the calculated total Bader charge analysis indicated charges on Fe in LFO, LSF55 and SFO were 2.00+, 2.03+ and 2.04+ respectively, while the calculated Bader charge on O became less negative as -1.36, -1.30, -1.21, respectively. If the Bader

charge is correct, it should be expected that with less negative charge on O (and essentially constant charge on Fe), the Fe-O bond will become weaker and the bond length will increase in going from LFO to SFO. However, the Fe-O bond length decreases from LFO to SFO (as shown in Table 1). If the charge on Fe changes from 3+ to 4+ from LFO to SFO, (as one might think from the incorrect but broadly used formal point charge and oxidation state analysis commonly employed by the Materials Science and Engineering research community) the Fe-O bond length should decrease, which is consistent with the computed and experimental bond lengths. This signifies that the calculated total Bader charge on O may be wrong and that on Fe was insensitive to the local electronic environment in LSF, and therefore was difficult to use, to determine the formal charge on Fe. Fortunately, the total unpaired electrons obtained via spin polarized Bader charge analysis of Fe show a significant variation from 3.88 to 4.64 *e* from SFO to LFO. Hence, the magnetic moment, which is a manifestation of the unpaired electrons in an element, was used to interpret the charge state on Fe. As we want to facilitate a comparison with experimentally predicted formal charge on Fe in LSF,[42] we have assumed localized electron on Fe and used magnetic moment interpreted charge comparable to spin polarized Bader charge. Accordingly, the magnetic moment calculated by VASP was used to interpret the formal charge state on Fe. Note, neither the spherical integration of charge used in a VASP calculation nor the Voronoi integration used in the Bader method gave the exact formal charge on Fe in LSF. Therefore, a magnetic moment of 4.23 μ_B for Fe was assigned to represent Fe^{3+} and 3.61 μ_B for Fe^{4+} in agreement with the LSF end member Fe charge states and magnetic moment discussed in Section 3.1a. It is possible that after neutral oxygen vacancy generation, some oxygen-vacancy-neighboring Fe^{3+} atoms will adopt a charge closer to Fe^{2+}. Although Fe^{2+} was not considered in the U-parameter selection, its charge was calibrated with the magnetic moment of Fe^{2+} in (planar) $SrFeO_2$. Since Fe^{2+} has the same number

of unpaired electrons as Fe^{4}+, it give rise to a magnetic moment of 3.68 μ_B which is close to the $\mu_{Fe^{4+}}$ = 3.61 μ_B (and comparable to experimentally reported $SrFeO_2$ magnetic moment at 10 K).[65]

Figure 3 shows the computed magnetic moment and the formal charge on Fe compared to the experimentally measured average charge on Fe in LSF, which also shows a linear relationship. Hence, in the current work an intermediate magnetic moment was interpreted as a linear interpolation between 3+ and 4+ charge states.[42] In LSF55, Fe is expected to carry a formal charge of 3.5+ and from the linear relation of charge and magnetic moment, $Fe^{3.5+}$ corresponds to a magnetic moment of 3.92 μ_B, which was very close to the VASP calculated magnetic moment of 3.94 μ_B for $Fe^{3.5+}$ in rhombohedral LSF55. Overall, the selection of U_{eff} = 3 and the magnetic moment interpreted charge jointly captured the Fe charge state ranging from Fe^{2+} to Fe^{4+} in $La_xSr_{1-x}FeO_{3-\square}$.

c) LSF Crystal Structures, Magnetic Ordering, and Band Gap at Low Temperature

Figure 1 shows the energetically favored crystal structures for LFO, SFO, and LSF55. In order to determine the ground state lattice structure for each LSF composition, three possible crystal structures each with two possible Fe magnetic ordering arrangements (ferromagnetic, FM, and anti-ferromagnetic, AFMG), were computed. From energy minimization, the stable, lowest-energy structures, presented in Table 2, were determined and illustrated in Figure 1. In Table 2, ΔE denotes the excess energy of a structure above the minimum energy of each composition, the 'μ_B' column denotes the magnetic moment on Fe in the structure, and the "tilt angle" denotes the Fe-O_6 octahedral tilt angle (which varies with the lattice structure and La/Sr ratio).

In accordance with experiments,[49] the orthorhombic (*Pbnm*) crystal structure with AFMG ordering was predicted as the stable LFO structure. The calculated lattice of 5.672 Å x 7.923 Å x

5.582 Å also compared well to the experimentally reported lattice parameters.[46,49] The Fe-O_6 octahedra in LFO showed a Z-out distortion (the b-axis in Figure 1a) with four 2.040 Å Fe-O bonds in the XY plane (the ac plane in Figure 1a) and two 2.057 Å bonds in the Z-direction (b-axis in Figure 1a). These Fe-O bond lengths are comparable to the experimentally measured average bond length of 2.006 Å.[46] The computed octahedral tilt was 154° (the bond angle of Fe-O-Fe) which was comparable to experimentally reported octahedral tilt of 157°.[46]

For stoichiometric SFO, the predicted phase is the experimentally reported low temperature cubic structure (space group: $Pm\bar{3}m$) with FM Fe ordering and a lattice parameter of 3.881 Å, which agreed well with experiments[55] (note, FM ordering was used to simplify the experimentally-reported helical Fe magnetic orientation arrangement in the 2K neutron diffraction SFO study of Reehuis *et al.).*[54] The predicted magnetic moment on Fe was 3.61 μ_B, which is similar to a literature DFT+U value of 3.7 μ_B calculated with U=5.4.[50] All the Fe-O bond lengths in SFO were equal to 1.940 Å due to octahedral (O_h) symmetry (Figure 1d) and were comparable to the experimentally reported bond length of 1.928 Å (measured at room temperature).[66]

For LSF55, the cubic, orthorhombic, rhombohedral structures were computed. The unit cell for rhombohedral LSF55 was depicted by a hexagonal lattice following the work of Kharton *et al*.[13] In light of the 0 to ~600K single phase behavior of LSF55 observed by X-ray diffraction[31,66,67] and the insensitive oxygen vacancy formation energy on the site ordering of La/Sr simulated by Ritzmann *et al.,*[10] an La/Sr ordered LSF55 phase was assumed. Thus, the 6*a* Wyckoff positions were assumed to be equally shared by La and Sr and an alternate layer of La-O and Sr-O was assumed, separated by the Fe-containing layer, as shown in Figure 1b. The present calculations correctly predicted that a hexagonal (rhombohedral) lattice structure with a *R32* space group is energetically favorable for LSF55. The calculated lattice length of the hexagonal unit cell

was a = 5.564 Å and c = 13.451 Å, and compared well with the experimental values (a = 5.5150 Å, c = 13.4287 Å).[13] In any octahedron, three of the calculated Fe-O bond lengths were 1.986 Å and the other three were 1.971 Å. Along the Fe-O-Fe-O direction, the Fe-O-Fe bond angle between two $Fe\text{-}O_6$ octahedra alternated between 166˚ and 161˚ and the Fe-O bond lengths also alternated between 1.986 and 1.971 Å. These calculated bond lengths are comparable to experimentally reported average Fe-O bond length of 1.954 Å (at room temperature).[66] Although it was predicted that FM order had a lower energy than AFM, the energy difference was only ~0.06 eV/f.u., and hence not in disagreement with the AFM magnetic orientation measured in LSF55 with Mössbauer spectroscopy at 78 K.[42]

Figure 4 shows the band gap for each energetically favored lattice structure. The partial density of states (PDOS) was calculated for both FM and AFMG ordering in LFO as shown in Figures 4a and 4b. The computed band gap was 0.5 and 2.0 eV for FM and AFMG ordering, respectively. The band gap predicted in AFMG LFO was comparable to the experimentally observed optical band gap of 2.1 eV measured at room temperature.[68] Cubic SFO shows a metallic behavior,[54] as correctly predicted in Figure 4e. The good match between the various predicted and measured properties for the other $SrFeO_{3-\square}$ phases can be found in our previous study.[19] The PDOS was calculated for both FM and AFMG magnetic ordering in LSF55 and reported in Figure 4c and 4d. Though there are few DOS observed close to Fermi energy with a FM orientation (Figure 4c), the AFMG ordered structure has an energy gap of 1.6 eV, comparable to earlier computational studies.[10]

Overall, the DFT settings successfully predicted that orthorhombic AFM, rhombohedral (hexagonal) (FM or AFM), and cubic (FM) were stable structures for LFO, LSF55, and SFO, respectively, at low temperature.

d) Choices of LSF Crystal Structures at SOFC Operating Temperature

Since, high temperature oxygen vacancy nonstoichiometry is important for SOFC applications, oxygen vacancy formation was studied in the high temperature LSF phases experimentally determined to be stable.[18,31] In terms of high temperature crystal structure, although LFO transforms from orthorhombic to rhombohedral at 1278±5 K (in air), rhombohedral LFO was not considered since the phase transition temperature is above typical SOFC operating temperatures. On the other hand, LSF55 shows a second order phase transition from rhombohedral to high-temperature cubic at around 523±50 K (in air).[31] For this reason, oxygen vacancy formation calculations were performed in both cubic and rhombohedral LSF55 phases. The rhombohedral LSF55 structure is shown in Figure 1c. SFO undergoes multiple vacancy ordering induced phase transitions as it progresses from cubic to tetragonal to orthorhombic to brownmillerite in a temperature range of 273 to 1273 K.[17] The oxygen vacancy formation calculations in these four SFO phases were performed by Das *et al.,*[19] and some of those computational results are presented in this paper for comparison. As shown in Figure 1, in all these structures, the perovskite (ABO_3) B-site (transition metal, here Fe) was coordinated to six oxygen atoms, forming an octahedral (Oh) Fe-O_6 coordination.[69] All the oxygen atoms were shared by two octahedra at their corners. After oxygen vacancy formation, the octahedral Fe adjacent to oxygen vacancy formation site went into Fe-O_5 square-pyramidal (SP) coordination.

In term of magnetic ordering, the Néel temperature for LFO is 750 K[49], and it is rapidly reduced with increasing Sr content. In fact, for LSF55 it is ~210 K,[47] and for SFO it is 133 K.[54] These Néel temperatures are much below the temperature range used for SOFC operation (and hence the oxygen vacancy site fraction calculations). Thus, Fe in all the LSF phases lose their

magnetic ordering and become paramagnetic (PM) at the SOFC operating temperature (>1000 K). However due to the computational complexity of modeling PM ordering, FM ordering was assumed on Fe,[19,29] for all oxygen vacancy formation calculations.

3.2 LSF Oxygen Vacancy Polaron Size and Shape

In this section, the vacancy formation sites and the oxidation state changes on Fe upon oxygen vacancy generation in various LSF phases were analyzed to determine the shape and size of the oxygen polarons shown in Figure 5. The Fe oxidation state changes on were explained by the electron occupancy and crystal-field-theory schematics shown in Figure 6.

a) $LaFeO_{3-\delta}$

In LFO, there are two different oxygen vacancy formation sites, one of which is between the long (2.057 Å) and short (2.040 Å) Fe-O bonds while the other one is between two short (2.040 Å) Fe-O bonds (Figure 1a). The oxygen vacancy formation calculations showed that the two-different oxygen vacancy formation sites have similar oxygen vacancy formation energies, differing by less than 0.01eV (i.e. within the energy resolution of the present study). The magnetic moment interpreted charge discussed in Section 3.1b showed that after oxygen vacancy formation, the two Fe atoms connected to the oxygen vacancy site changed their charge states from 3+ to 2.3+, while all the other Fe atoms in the lattice maintained their charge at 3+ (as in perfect LFO). This indicates that after oxygen vacancy formation, the excess electrons generated by neutral oxygen vacancy formation remained localized to the oxygen vacancy adjacent area and formed a relatively small polaron, as shown by Figure 5a. Bader charge analysis before and after oxygen vacancy formation also shows the charge localization on vacancy adjacent Fe in LFO. The total

Bader charge on oxygen vacancy adjacent Fe changed by more than 0.5 *e* but the charge change from total Bader analysis on other neighboring atoms (including La, Fe, and O) was less than 0.05 *e*. This charge localization can be simply explained by the electronic distribution on the oxygen-vacancy-adjacent Fe *d*-orbitals. According to crystal field theory, the Fe *d*-orbitals in the octahedral coordination found in the perfect LFO lattice split into $t_{2g}^3e_g^2$, which can be further split into $b_{2g}^1e_g^2b_{1g}^1a_{1g}^1$ due to Jahn-Teller distortions, as shown in Figure 6a. All the Fe atoms in perfect LFO are in the 3+ high-spin state with each Fe containing five electrons in its *3d* orbital ([Ar] $3d^5$), indicated by the blue arrows in Figure 6a. As a geometric consequence of losing a neighboring oxygen during oxygen vacancy formation, the two first-nearest-neighboring Fe atoms become SP coordinated, creating a different *d* orbital splitting situation of $e_g^2b_{2g}^1a_{1g}^1b_{1g}^1$. To minimize the system energy, the two electrons produced during neutral oxygen vacancy formation are distributed to the lowest energy level of *d*-orbitals of each Fe in the SP coordination. Hence, in LFO the excess (i.e. polaron) electrons remain localized and adjacent to the oxygen vacancy site. A schematic of the polaron (shown in yellow in Figure 5a and with a perspective view of oxygen vacancy adjacent lattice area in Figure 5e), show the resulting small $LaFeO_{3-\delta}$ polaron which is elongated along the Z direction with a length of ~4.0 Å.

b) $SrFeO_{3-\delta}$

In cubic SFO, the electrons produced by a neutral oxygen vacancy formation do not remain localized on the first-nearest-neighboring Fe connected to the oxygen vacancy. According to total Bader charge analysis charge change on Fe after the formation of oxygen vacancy in SFO was insignificant (less than 0.1 *e*). Whereas, spin polarized Bader charge calculation shows the change of charge on the second nearest neighboring Fe was close to 0.1 *e*. Charge change on Sr after the

formation of oxygen vacancy was less than 0.03 *e* (insignificant). So, there is no impact of oxygen vacancy polaron on Sr. According to the magnetic moment interpreted charge, the charge on two Fe connected to the oxygen vacancy site increased by 0.2+ and the charge on the eight second-nearest-neighboring Oh-Fe reduced by 0.2+.[19] The reason for this long-range charge transfer can also be explained by the electron distribution in the Fe 3*d*-orbitals split in different Fe-O polyhedra. Specifically, before oxygen vacancy formation, the electron *d*-orbital distribution of Oh-Fe^{4+} is $t_{2g}^3e_g^1$ (as there is no octahedral distortion in perfect SFO).[19,70] The Fe in perfect SFO has an [Ar] $3d^4$ 4+ charge state, i.e., 4 electrons in the *3d* orbitals, as indicated by the blue arrows in Figure 6b. After oxygen vacancy formation, the excess electrons generated due to oxygen vacancy formation (i.e. the red arrows in Figure 6b) transfer to a_{1g} level in the Oh-Fe atoms instead of a higher energy b_{1g} of the nearest-neighbor, SP-coordinated Fe ions. Further, since there are eight second-nearest neighboring Oh-Fe present with the same a_{1g} energy level around each oxygen vacancy site, the excess electrons are distributed between these eight Fe atoms to produce the "pancake" shaped polaron shown in Figures 5d and 5h with an estimated polaron diameter and height of ~7.8 and ~3.9 Å, respectively.

c) Rhombohedral and Cubic $La_{0.5}Sr_{0.5}FeO_{3-\delta}$

In both stoichiometric rhombohedral and stoichiometric cubic LSF55, the computationally predicted charge state on Fe is 3.5+. This indicates that, on average, formally there are four and a half electrons in the Fe *d*-orbitals. One could imagine, as a combination of LFO and SFO, the excess electrons due to oxygen vacancy formation could therefore be distributed to both the first and second nearest neighboring Fe atoms and this is indeed the case, as shown in Figures 5f and 5g.

In cubic LSF55, after oxygen vacancy formation all the Oh-Fe connected to the SP-Fe via two 180˚ Fe-O-Fe bonds bend to 160º. The charge on first and second nearest neighboring Fe atoms were 3.35+, suggesting that the electrons left behind by neutral oxygen vacancy formation were distributed to the first (two SP-Fe) and second (eight Oh-Fe) nearest neighboring Fe atoms to the oxygen vacancy. Thus, as shown in Figures 5c and 5g, in cubic LSF55 the oxygen vacancy polaron exhibit a "pancake" shaped polaron with an average diameter and height of ~8.3 and ~4.0 Å, respectively.

In rhombohedral LSF55, the polaron size is smaller than that in cubic LSF55, due to a larger Fe-O polyhedra tilt angle in the rhombohedral structure. The oxygen vacancy formation calculations showed that oxygen vacancy formation in the Sr-O_3 plane was energetically favorable, compared to oxygen vacancy formation in the La-O_3 plane, by ~0.1 eV. After oxygen vacancy formation, the two SP Fe charge changed to 3.6+ from 3.5+. In contrast, the four Oh-Fe connected with the tilted Fe-O-Fe bond shown in Figure 5c gained electrons and became 3.3+ from 3.5+. This difference is related to the Fe-O-Fe bond angle. Note there are four Oh-Fe connecting the four O atoms at the square bottom of the SP-Fe polyhedra, via a Fe-O-Fe bridge. In rhombohedral LSF55, two of the Fe-O-Fe bond angles are ~170º (compared to 180˚ in the cubic structure) and the other two Fe-O-Fe bond angles are ~153º (i.e they are more bent). Since a more bent bond angle results in more Jahn-Teller distortions, the split e_g energy level in the more tilted Oh will be at a lower energy state and the excess electrons generated by oxygen vacancy formation will preferably transfer to the more titled Oh-Fe atoms, as shown in Figures 5c and 5g. In rhombohedral LSF55, these excess electrons produced a quarter of a "pancake" like polaron shape (Figure 5f). The polaron size was approximately one-fourth of that in cubic LSF55, with an average polaron radius and height of 4.3 and 4.0 Å, respectively.

As shown in Figure 5, the size of the polaron is the smallest in LFO and it increases with increasing Sr doping LSF. The small and more localized polaron in LFO can screen the charge of the oxygen vacancy more effectively, thus the oxygen vacancies will remain non-interacting and will not impact each other's polaronic strain field, until they are very close. However, the larger and more delocalized polarons can not screen the vacancy charge effectively, and thus the vacancies may start to interact, even at a large distance. Therefore, in the next section, the oxygen vacancy formation energy as a function of vacancy concentration was studied and correlated with the polaron size.

3.3 The Influence of the Oxygen Vacancy Concentration on the Oxygen Vacancy Formation Energy

In Figure 7, the DFT+U calculated oxygen vacancy formation energies for various LSF phases are plotted versus increasing oxygen non-stoichiometry per formula unit (i.e δ). The vacancy formation energies in LFO remained constant at 3.57 ± 0.04 eV and did not show any significant interaction even at high oxygen non-stoichiometry (i.e. at $\delta = 0.25$). This is consistent with the small and localized vacancy LFO polaron that allows the oxygen vacancies to be very close without interacting (and hence treated as dilute).

After exhibiting dilute behavior at low δ, the vacancy formation energy in cubic SFO increased with increasing δ. As shown in Figure 7, the vacancy formation energy remained constant at ~0.4 eV up to a $\delta = 0.05$ when the oxygen vacancies were more than 11 Å apart. With a $\delta > 0.05$ a weak interaction among vacancies was observed. This interaction can be explained by the fact that at an oxygen non-stoichiometry $\delta = 0.05$ the average distance between the oxygen vacancies is ~ 8-11 Å, at which point the ~7.8 Å diameter cubic SFO polarons begin to

overlap/interact. At a δ> 0.1 strong interactions begin which produce a fast increase in the vacancy formation energy (since the vacancies are closer than 8 Å). Furthermore, the anisotropic pancake-shaped polaron will likely lead to a preferred vacancy arrangement, thus contributing to the oxygen vacancy ordering induced phase changes from cubic → tetragonal → orthorhombic → brownmillerite known to occur in SFO with increasing oxygen non-stoichiometry.[17]

Figure 7 also shows that rhombohedral LSF55, which as shown in Figure 5 has tilted Fe-O polyhedra and a small polaron size compared to the untilted Fe-O polyhedra and large polaron sizes found in cubic LSF55, exhibits a lower oxygen vacancy formation energy and less oxygen vacancy interactions than cubic LSF55. The vacancy formation energy in rhombohedral LSF55 remained constant at ~1.7 eV for $\delta \leq 0.25$ until the polarons began to overlap at an average distance between oxygen vacancies of ~7 Å, larger than the polaron size due to its irregular shape. In contrast, cubic LSF55 showed an increasing trend even for δ <0.1, due to its much larger polaron size. Note, in cubic LSF55 it was not computationally possible to find a dilute limit for oxygen vacancy formation. This is because the atomic position relaxation of the cubic LSF55 supercell with very low oxygen non-stoichiometry (δ = 0.03) resulted in increased octahedral tilt around each oxygen vacancy site producing a locally rhombohedral LSF55 structure. According to the ΔE_{vac}^{f} defined in Equation 4, this local phase transformation decreased the $E_{defective}^{DFT}$, so the ΔE_{vac}^{f} was reduced as well. This resulted in the calculated cubic LSF55 oxygen vacancy formation energy that was less than that found in rhombohedral LSF55 (1.4 eV vs. 1.7 eV) at very low oxygen non-stoichiometry. The cubic to rhombohedral phase change near an oxygen vacancy is consistent with the low temperature (0K) stability of the rhombohedral phase, shown in Table II. This transition suggests that cubic LSF55 may only exist at higher δ. This is also consistent with the experimental

observation that the LSF55 rhombohedral to cubic phase transformation occurs with increasing temperature,[31] when δ is high.

Overall, the oxygen vacancy formation energies in rhombohedral and cubic LSF55 suggest that smaller polaron size leads to weaker interaction among oxygen vacancies. Further, the observed trends with La:Sr ratio indicate that progressively larger polaron sizes result in increasing oxygen vacancy formation energies with increasing Sr or δ. This behavior is consistent with experimental results showing that Sr-rich LSF and highly oxygen deficient compositions are more prone to oxygen-vacancy-ordering-induced phase transformations, while Sr-poor and oxygen rich LSF compositions are not.[22]

In addition, the crystal-field-theory based polaron size estimation technique presented here can be applied to other perovskite structures. For example, $LaMnO_3$ has a structure similar to $LaFeO_3$, which shows almost no oxygen vacancy interactions. However, Mn^{3+} has the same number of d-electrons as Fe^{4+} (i.e. both have an electron configuration of [Ar] $3d^4$). Therefore, the excess electrons generated by oxygen vacancy formation should be distributed to the Oh-coordinated Fe, and thus the long-range charge transfer observed in $SrFeO_3$ should also occur in $LaMnO_3$ and result in a large oxygen vacancy polaron size that leads to strong vacancy interactions that cause the increasing vacancy formation energy with □, as reported by Lee *et al*.[20]

3.4 Comparison of the Oxygen Vacancy Site Fractions in LSF from 0 to 1000ºC

Figure 8 shows the oxygen vacancy site fraction as a function of temperature and partial pressure of oxygen (p_{O2} = 0.21 atm) for three different LSF compositions calculated using the non-dilute oxygen vacancy site fraction calculation method of Equation 6. This method was developed and used in our earlier study[19] to predict the □ and X as a function of temperature in SFO in air,

and (considering phase changes in the material) the predicted trends compared well with the experimental TGA data.

Figure 8a compares the calculated oxygen vacancy non-stoichiometry, δ, in rhombohedral and cubic LSF55 structures with experimentally measured data[71] and shows reasonably good agreement at SOFC operating temperatures (600 ˚C ~1200 ˚C) The experimental data in Figure 8a also shows that for LSF55 the slope of the □ □vs temperature relation decreases with increasing temperature. This is caused by rhombohedral to cubic phase transformation at high temperature[31] and the stronger oxygen vacancy interactions in cubic LSF55 than in rhombohedral LSF55 at low temperature. As discussed previously, rhombohedral LSF55 generally has a lower oxygen vacancy formation energy, and therefore Figure 8a shows a higher □ □for rhomohedral LSF than for cubic LSF at similar temperatures. The rhomohedral to cubic LSF phase transformation temperature increases with higher La:Sr ratio, as shown in the experimentally overlaid phase diagrams of Figure 8c. For example, the phase transition temperature occurs at ~450ºC for LSF55 but is increased to 800˚C for $La_{0.6}Sr_{0.4}FeO_{3-\delta}$ (LSF64). Hence, it is beneficial to adjust the La:Sr ratio so that a highly oxygen deficient rhombohedral LSF, instead of cubic LSF, is formed. This likely contributes to the high performance of $La_{0.6}Sr_{0.4}FeO_{3-\delta}$ (LSF64) at traditional 800ºC SOFC operation, as LSF64 retains the rhombohedral phase at 800ºC according to the experimental phase diagram,

Considering the various phase transitions occurring in LSF, the oxygen vacancy site fraction, *X*, was computed for the specific phase occurring at that temperature according to the experimental phase diagrams from Fossdal *et al.,*[31] and Takeda *et al*.[17] The computed *X* values for LFO, SFO, and LSF55 are plotted in Figure 8b. Figure 8b shows that, due to the oxygen vacancy formation energies shown in Figure 7 and those calculated for other phases, increasing La:Sr ratio

tends to result in a lower *X* at a given temperature. In LFO, there were almost no oxygen vacancy sites till 1000ºC. In contrast, SFO is highly oxygen deficient SFO, but experiences a reduction in *X* with increasing temperature due to oxygen vacancy ordering once brownmillerite is formed. Figure 8b also shows that the *X* in orthorhombic $SrFeO_{3-\square}$, is larger than in LSF55 at ~600ºC. Additional studies on the oxygen ion conductivity are underway to determine if this results in a higher ~600ºC SFO ionic conductivity than LSF55.[11,72]

4. CONCLUSIONS

To elucidate the effect of oxygen vacancy polaron shape and size on the vacancy interaction in LSF, three different LSF compositions were computationally studied with GGA+U. The selection of a Hubbard-*U* (= 3) parameter was calibrated in order to predict the magnetic moment on Fe as a function of La/Sr ratio and oxygen non-stoichiometry. The magnetic moment on Fe was utilized to interpret the formal charge on Fe. The oxidation state change on Fe upon oxygen vacancy generation outlined the shape and size of the oxygen polarons. It was found that in $LaFeO_3$ the excess electrons produced during oxygen vacancy formation were localized at the Fe atoms adjacent to the oxygen vacancy, resulting in a small polaron. In contrast, in $SrFeO_3$ the excess electrons produced during oxygen vacancy formation were transferred to the second-nearest-neighbor Fe atoms, resulting in a pancake-shaped large polarons. This difference is well explained by the electron occupancy and crystal-field-splitting-induced differences between the Fe *3d*-orbitals of the square pyramidally coordinated, oxygen-vacancy-adjacent Fe atoms and the octahedrally-coordinated, oxygen-vacancy-second-nearest-neighbor Fe atoms. For $La_{0.5}Sr_{0.5}FeO_{3-\delta}$, the polaron size in the rhombohedral phase was smaller than that in cubic phase, due to the tilt of $Fe\text{-}O_6$ octahedra. In all cases, larger oxygen vacancy polarons resulted in higher oxygen vacancy

interactions. In fact, in multiple phases, the oxygen vacancy formation energy started to increase with oxygen non-stoichiometry beyond a critical value when the polarons began to overlap.

Overall, the calculated polaron shape changes and progressively increased polaron sizes with increasing Sr or δ, resulted in increasing oxygen vacancy formation energies in $La_{1-x}Sr_xFeO_{3-\delta}$. This was consistent with experimental results showing that Sr-rich LSF and highly oxygen deficient compositions are more prone to oxygen-vacancy-ordering-induced phase transformations, while Sr-poor and oxygen rich LSF compositions are not. Since oxygen vacancy induced phase transformations cause a decrease in the mobile oxygen vacancy site fraction (X), both δ and X were also predicted as a function of temperature and oxygen partial pressure, for multiple LSF compositions and phases using a combined thermodynamics and DFT approach. Consistent with its superior electrochemical performance, rhombohedral LSF was found to have the smaller polaron size and a greater X than cubic LSF at identical temperatures.

In summary, this work has shown for the first time how transition metal d-orbital splitting affects the size of oxygen vacancy polarons, which in turn determines how oxygen deficient a material can become before it encounters an oxygen-vacancy-induced phase change. In addition to clarifying how today's best MIEC materials behave, these new insights will likely be important for the bottom-up design of next-generation ionic conducting materials.

Acknowledgements

TD and YQ acknowledge support from National Science Foundation Award Number DMR-1410850 and JDN acknowledges support from National Science Foundation CAREER Award Number CBET-1254453. All the calculations reported here were performed at the High Performance Computing Center at Michigan State University.

References:

(1) Baumann, F. S.; Fleig, J.; Cristiani, G.; Stuhlhofer, B.; Habermeier, H.-U.; Maier, J. Quantitative Comparison of Mixed Conducting SOFC Cathode Materials by Means of Thin Film Model Electrodes. *J. Electrochem. Soc.* **2007**, *154* (9), B931–B941.

(2) Nicholas. J. D. Highlights from the 2013 National Science Foundation Solid Oxide Fuel Cell Promise, Progress, and Priorities (SOFC-PPP) Workshop. *Electrochem. Soc. Interface* **2013**, No. Winter 2013, 49.

(3) Yang, Q.; Burye, T. E.; Lunt, R. R.; Nicholas, J. D. In Situ Oxygen Surface Exchange Coefficient Measurements on Lanthanum Strontium Ferrite Thin Films via the Curvature Relaxation Method. *Solid State Ionics.* **2013**, *249–250* (0), 123–128.

(4) Burye, T. E.; Tang, H.; Nicholas, J. D. The Effect of Precursor Solution Desiccation or Nano-Ceria Pre-Infiltration on Various $La_{0.6}Sr_{0.4}Fe_yCo_{1-y}O_{3-x}$ Infiltrate Compositions. *J. Electrochem. Soc.* **2016**, *163* (9), F1017–F1022.

(5) Yadav, A. K.; Singh, R. K.; Singh, P. Fabrication of Lanthanum Ferrite Based Liquefied Petroleum Gas Sensor. *Sens. Actuators B Chem.* **2016**, *229*, 25–30.

(6) Brisotto, M.; Cernuschi, F.; Drago, F.; Lenardi, C.; Rosa, P.; Meneghini, C.; Merlini, M.; Rinaldi, C. High Temperature Stability of $Ba_{0.5}Sr_{0.5}Co_{0.8}Fe_{0.2}O_{3-\delta}$ and $La_{0.6}Sr_{0.4}Co_{1-y}Fe_yO_{3-\delta}$ Oxygen Separation Perovskite Membranes. *J. Eur. Ceram. Soc.* **2016**, *36* (7), 1679–1690.

(7) Magyari-Köpe, B.; Park, S. G.; Lee, H.-D.; Nishi, Y. First Principles Calculations of Oxygen Vacancy-Ordering Effects in Resistance Change Memory Materials Incorporating Binary Transition Metal Oxides. *J. Mater. Sci.* **2012**, *47* (21), 7498–7514.

(8) Kuklja, M. M.; Kotomin, E. A.; Merkle, R.; Mastrikov, Y. A.; Maier, J. Combined Theoretical and Experimental Analysis of Processes Determining Cathode Performance in Solid Oxide Fuel Cells. *Phys. Chem. Chem. Phys.* **2013**, *15* (15), 5443.

(9) Mizusaki, J.; Sasamoto, T.; Cannon, W. R.; Bowen, H. K. Electronic Conductivity, Seebeck Coefficient, and Defect Structure of $La_{1-x}Sr_xFeO_3$ (x=0.l, 0.25). *J. Am. Ceram. Soc.* **1983**, *66* (4), 247–252.

(10) Ritzmann, A. M.; Muñoz-García, A. B.; Pavone, M.; Keith, J. A.; Carter, E. A. Ab Initio DFT+U Analysis of Oxygen Vacancy Formation and Migration in $La_{1-x}Sr_xFeO_{3-\delta}$ = 0, 0.25, 0.50). *Chem. Mater.* **2013**, *25* (15), 3011–3019.

(11) Das, T.; Nicholas, J. D.; Qi, Y. First-Principles Studies of Oxygen Vacancy Interactions and Their Impact on Oxygen Migration in Lanthanum Strontium Ferrite. *ECS Trans.* **2017**, *78* (1), 2807–2814.

(12) Choi, S.; Yoo, S.; Kim, J.; Park, S.; Jun, A.; Sengodan, S.; Kim, J.; Shin, J.; Jeong, H. Y.; Choi, Y.; Kim, G.; Liu, M. Highly Efficient and Robust Cathode Materials for Low-Temperature Solid Oxide Fuel Cells: $PrBa_{0.5}Sr_{0.5}Co_{2-x}Fe_xO_{5+\delta}$. *Sci. Rep.* **2013**, *3*.

(13) Kharton, V. V.; Kovalevsky, A. V.; Patrakeev, M. V.; Tsipis, E. V.; Viskup, A. P.; Kolotygin, V. A.; Yaremchenko, A. A.; Shaula, A. L.; Kiselev, E. A.; Waerenborgh, J. C. Oxygen Nonstoichiometry, Mixed Conductivity, and Mössbauer Spectra of $Ln_{0.5}A_{0.5}FeO_{3-\delta}$ (Ln = La−Sm, A = Sr, Ba): Effects of Cation Size. *Chem. Mater.* **2008**, *20* (20), 6457–6467.

(14) Fuks, D.; Mastrikov, Y.; Kotomin, E.; Maier, J. Ab Initio Thermodynamic Study of (Ba,Sr)(Co,Fe)O_3 Perovskite Solid Solutions for Fuel Cell Applications. *J. Mater. Chem. A* **2013**, *1* (45), 14320.

(15) Mizusaki, J.; Yoshihiro, M.; Yamauchi, S.; Fueki, K. Nonstoichiometry and Defect Structure of the Perovskite-Type Oxides $La_{1-x}Sr_xFeO_{3-\delta}$. *J. Solid State Chem.* **1985**, *58* (2), 257–266.

(16) Patrakeev, M. V.; Bahteeva, J. A.; Mitberg, E. B.; Leonidov, I. A.; Kozhevnikov, V. L.; Poeppelmeier, K. R. Electron/Hole and Ion Transport in $La_{1-x}Sr_xFeO_{3-\delta}$. *J. Solid State Chem.* **2003**, *172* (1), 219–231.

(17) Takeda, Y.; Kanno, K.; Takada, T.; Yamamoto, O.; Takano, M.; Nakayama, N.; Bando, Y. Phase Relation in the Oxygen Nonstoichiometric System, $SrFeO_x$ ($2.5 \leq x \leq 3.0$). *J. Solid State Chem.* **1986**, *63* (2), 237–249.

(18) Mizusaki, J.; Okayasu, M.; Yamauchi, S.; Fueki, K. Nonstoichiometry and Phase Relationship of the $SrFeO_{2.5}$-$SrFeO_3$ System at High Temperature. *J. Solid State Chem.* **1992**, *99* (1), 166–172.

(19) Das, T.; Nicholas, J. D.; Qi, Y. Long-Range Charge Transfer and Oxygen Vacancy Interactions in Strontium Ferrite. *J. Mater. Chem. A* **2017**, *5* (9), 4493–4506.

(20) Lee, Y.-L.; Morgan, D. Ab Initio and Empirical Defect Modeling of $LaMnO_{3\pm\delta}$ for Solid Oxide Fuel Cell Cathodes. *Phys Chem Chem Phys* **2012**, *14* (1), 290–302.

(21) Kuklja, M. M.; Mastrikov, Y. A.; Jansang, B.; Kotomin, E. A. The Intrinsic Defects, Disordering, and Structural Stability of $Ba_xSr_{1-x}Co_yFe_{1-y}O_{3-\delta}$ Perovskite Solid Solutions. *J. Phys. Chem. C* **2012**, *116* (35), 18605–18611.

(22) Bahteeva, J. A.; Leonidov, I. A.; Patrakeev, M. V.; Mitberg, E. B.; Kozhevnikov, V. L.; Poeppelmeier, K. R. High-Temperature Ion Transport in $La_{1-x}Sr_xFeO_{3-\delta}$. *J. Solid State Electrochem.* **2004**, *8* (9), 578–584.

(23) Landau, L. D. Über die Bewegung der Elektronen in Kristalgitter. *Phys Z Sowjetunion* **1933**, *3*, 644–645.

(24) Jung, W.-H. Transport Mechanisms in $La_{0.7}Sr_{0.3}FeO_3$: Evidence for Small Polaron Formation. *Phys. B Condens. Matter* **2001**, *299* (1), 120–123.

(25) Castleton, C. W. M.; Lee, A. L.; Kullgren, J.; Hermansson, K. Description of Polarons in Ceria Using Density Functional Theory. *J. Phys. Conf. Ser.* **2014**, *526* (1), 012002.

(26) Das, T.; Nicholas, J. D.; Qi, Y. In Preparation: Anisotropic Chemical Expansion in Nonstoichiometric Ceria. **2017**.

(27) Ishigaki, T.; Yamauchi, S.; Kishio, K.; Mizusaki, J.; Fueki, K. Diffusion of Oxide Ion Vacancies in Perovskite-Type Oxides. *J. Solid State Chem.* **1988**, *73* (1), 179–187.

(28) Taylor, D. D.; Schreiber, N. J.; Levitas, B. D.; Xu, W.; Whitfield, P. S.; Rodriguez, E. E. Oxygen Storage Properties of $La_{1-x}Sr_xFeO_{3-\delta}$ for Chemical-Looping Reactions—An In Situ Neutron and Synchrotron X-Ray Study. *Chem. Mater.* **2016**, *28* (11), 3951–3960.

(29) Mastrikov, Y. A.; Merkle, R.; Kotomin, E. A.; Kuklja, M. M.; Maier, J. Formation and Migration of Oxygen Vacancies in $La_{1-x}Sr_xCo_{1-y}Fe_yO_{3-\delta}$ Perovskites: Insight from Ab Initio Calculations and Comparison with $Ba_{1-x}Sr_xCo_{1-y}Fe_yO_{3-\delta}$. *Phys Chem Chem Phys* **2013**, *15* (3), 911–918.

(30) Dann, S. E.; Currie, D. B.; Weller, M. T.; Thomas, M. F.; Al-Rawwas, A. D. The Effect of Oxygen Stoichiometry on Phase Relations and Structure in the System $La_{1-x}Sr_xFeO_{3-\delta}$ ($0 \leq x \leq 1$, $0 \leq \delta \leq 0.5$). *J. Solid State Chem.* **1994**, *109* (1), 134–144.

(31) Fossdal, A.; Menon, M.; Wærnhus, I.; Wiik, K.; Einarsrud, M.-A.; Grande, T. Crystal Structure and Thermal Expansion of $La_{1-x}Sr_xFeO_{3-\delta}$ Materials. *J. Am. Ceram. Soc.* **2004**, *87* (10), 1952–1958.

(32) Taylor, F. H.; Buckeridge, J.; Catlow, C. R. A. Defects and Oxide Ion Migration in the Solid Oxide Fuel Cell Cathode Material $LaFeO_3$. *Chem. Mater.* **2016**, *28* (22), 8210–8220.

(33) Lee, C.-W.; Behera, R. K.; Wachsman, E. D.; Phillpot, S. R.; Sinnott, S. B. Stoichiometry of the $LaFeO_3$ (010) Surface Determined from First-Principles and Thermodynamic Calculations. *Phys. Rev. B* **2011**, *83* (11), 115418.

(34) Dudarev, S. L.; Botton, G. A.; Savrasov, S. Y.; Humphreys, C. J.; Sutton, A. P. Electron-Energy-Loss Spectra and the Structural Stability of Nickel Oxide: An LSDA+U Study. *Phys. Rev. B* **1998**, *57* (3), 1505–1509.

(35) Jain, A.; Hautier, G.; Ong, S. P.; Moore, C. J.; Fischer, C. C.; Persson, K. A.; Ceder, G. Formation Enthalpies by Mixing GGA and GGA + U Calculations. *Phys. Rev. B* **2011**, *84* (4), 045115.

(36) Wang, L.; Maxisch, T.; Ceder, G. Oxidation Energies of Transition Metal Oxides within the GGA+U Framework. *Phys. Rev. B* **2006**, *73* (19), 195107.

(37) Ceder, G.; Hautier, G.; Jain, A.; Ong, S. P. Recharging Lithium Battery Research with First-Principles Methods. *MRS Bull.* **2011**, *36* (3), 185–191.

(38) Anisimov, V. I.; Aryasetiawan, F.; Lichtenstein, A. I. First-Principles Calculations of the Electronic Structure and Spectra of Strongly Correlated Systems: The LDA+ U Method. *J. Phys. Condens. Matter* **1997**, *9* (4), 767.

(39) Mosey, N. J.; Liao, P.; Carter, E. A. Rotationally Invariant Ab Initio Evaluation of Coulomb and Exchange Parameters for DFT+U Calculations. *J. Chem. Phys.* **2008**, *129* (1), 014103.

(40) Akriche, A.; Bouafia, H.; Hiadsi, S.; Abidri, B.; Sahli, B.; Elchikh, M.; Timaoui, M. A.; Djebour, B. First-Principles Study of Mechanical, Exchange Interactions and the Robustness in Co_2MnSi Full Heusler Compounds. *J. Magn. Magn. Mater.* **2017**, *422*, 13–19.

(41) Bentouaf, A.; Mebsout, R.; Rached, H.; Amari, S.; Reshak, A. H.; Aïssa, B. Theoretical Investigation of the Structural, Electronic, Magnetic and Elastic Properties of Binary Cubic C15-Laves Phases TbX_2 (X = Co and Fe). *J. Alloys Compd.* **2016**, *689*, 885–893.

(42) Gallagher, P. K.; MacChesney, J. B. Mössbauer Effect in the System $Sr_{1-x}La_xFeO_3$. *Symp Faraday Soc* **1967**, *1* (0), 40–47.

(43) David Sholl; Janice A Steckel. *Density Functional Theory: A Practical Introduction*, April 2009.; WILEY, 2009.

(44) Zhang, W.; Smith, J. R.; Wang, X. G. Thermodynamics from Ab Initio Computations. *Phys. Rev. B* **2004**, *70* (2), 024103.

(45) Reuter, K.; Scheffler, M. Composition, Structure, and Stability of RuO_2(110) as a Function of Oxygen Pressure. *Phys. Rev. B* **2001**, *65* (3), 035406.

(46) Marezio, M.; Dernier, P. D. The Bond Lengths in $LaFeO_3$. *Mater. Res. Bull.* **1971**, *6* (1), 23–29.

(47) Shimony, U.; Knudsen, J. M. Mössbauer Studies on Iron in the Perovskites $La_{1-x}Sr_xFeO_3$ (0<~x<~1). *Phys. Rev.* **1966**, *144* (1), 361–366.

(48) Gryaznov, D.; Heifets, E.; Kotomin, E. The First-Principles Treatment of the Electron-Correlation and Spin–orbital Effects in Uranium Mononitride Nuclear Fuels. *Phys. Chem. Chem. Phys.* **2012**, *14* (13), 4482–4490.

(49) Koehler, W. C.; Wollan, E. O. Neutron-Diffraction Study of the Magnetic Properties of Perovskite-like Compounds $LaBO_3$. *J. Phys. Chem. Solids* **1957**, *2* (2), 100–106.

(50) Shein, I. R.; Shein, K. I.; Kozhevnikov, V. L.; Ivanovskii, A. L. Band Structure and the Magnetic and Elastic Properties of $SrFeO_3$ and $LaFeO_3$ Perovskites. *Phys. Solid State* **2005**, *47* (11), 2082–2088.

(51) Zhang, Q.; Yunoki, S. A First-Principles Study for Electronic and Magnetic Properties of $LaFeO_3$ /$LaCrO_3$ Superlattices. *J. Phys. Conf. Ser.* **2012**, *400* (3), 032126.

(52) Hoffmann, A.; Seo, J. W.; Fitzsimmons, M. R.; Siegwart, H.; Fompeyrine, J.; Locquet, J.-P.; Dura, J. A.; Majkrzak, C. F. Induced Magnetic Moments at a Ferromagnet-Antiferromagnet Interface. *Phys. Rev. B* **2002**, *66* (22), 220406.

(53) Takano, M.; Takeda, Y. Electronic State of Fe^{4+} Ions in Perovskite-Type Oxides. *Bull. Inst. Chem. Res. Kyoto Univ.* **1983**, *61* (5–6), 406–425.

(54) Reehuis, M.; Ulrich, C.; Maljuk, A.; Niedermayer, C.; Ouladdiaf, B.; Hoser, A.; Hofmann, T.; Keimer, B. Neutron Diffraction Study of Spin and Charge Ordering in $SrFeO_{3-\delta}$. *Phys. Rev. B* **2012**, *85* (18), 184109.

(55) Hodges, J. P.; Short, S.; Jorgensen, J. D.; Xiong, X.; Dabrowski, B.; Mini, S. M.; Kimball, C. W. Evolution of Oxygen-Vacancy Ordered Crystal Structures in the Perovskite Series $Sr_nFe_nO_{3n-1}$ (n=2, 4, 8, and ∞), and the Relationship to Electronic and Magnetic Properties. *J. Solid State Chem.* **2000**, *151* (2), 190–209.

(56) Xiao, G.; Liu, Q.; Wang, S.; Komvokis, V. G.; Amiridis, M. D.; Heyden, A.; Ma, S.; Chen, F. Synthesis and Characterization of Mo-Doped $SrFeO_{3-\delta}$ as Cathode Materials for Solid Oxide Fuel Cells. *J. Power Sources* **2012**, *202*, 63–69.

(57) Takeda, T; Komura, S; Watanabe, N. In *FERRITES: Proc. Int. Conf. Sept.-Oct. 1980*; Center for Academic Publication, Japan: Japan; p 385.

(58) Watanabe, H.; Oda, H.; Nakamura, E.; Yamaguchi, Y.; Takei, H. In *FERRITES: Proc. Int. Conf. Sept.-Oct. 1980*; Center for Academic Publication, Japan: Japan; p 381.

(59) Takeda, T.; Watanabe, T.; Komura, S.; Fujii, H. Magnetic Properties of $SrFe_{1-x}Co_xO_3$. *J. Phys. Soc. Jpn.* **1987**, *56* (2), 731–735.

(60) Muñoz-García, A. B.; Pavone, M.; Carter, E. A. Effect of Antisite Defects on the Formation of Oxygen Vacancies in Sr_2FeMoO_6: Implications for Ion and Electron Transport. *Chem. Mater.* **2011**, *23* (20), 4525–4536.

(61) Yang, Z.; Huang, Z.; Ye, L.; Xie, X. Influence of Parameters U and J in the LSDA+U Method on Electronic Structure of the Perovskites $LaMO_3$ (M=Cr,Mn,Fe,Co,Ni). *Phys. Rev. B* **1999**, *60* (23), 15674–15682.

(62) Muñoz-García, A. B.; Pavone, M.; Ritzmann, A. M.; Carter, E. A. Oxide Ion Transport in $Sr_2Fe_{1.5}Mo_{0.5}O_{6-\delta}$, a Mixed Ion-Electron Conductor: New Insights From First Principles Modeling. *Phys. Chem. Chem. Phys.* **2013**, *15* (17), 6250.

(63) Tang, W.; Sanville, E.; Henkelman, G. A Grid-Based Bader Analysis Algorithm without Lattice Bias. *J. Phys. Condens. Matter* **2009**, *21* (8), 084204.

(64) Bouibes, A.; Zaoui, A. High-Pressure Polymorphs of $ZnCO_3$: Evolutionary Crystal Structure Prediction. *Sci. Rep.* **2014**, *4*.

(65) Tsujimoto, Y.; Tassel, C.; Hayashi, N.; Watanabe, T.; Kageyama, H.; Yoshimura, K.; Takano, M.; Ceretti, M.; Ritter, C.; Paulus, W. Infinite-Layer Iron Oxide with a Square-Planar Coordination. *Nature* **2007**, *450* (7172), 1062–1065.

(66) Haas, O.; Vogt, U. F.; Soltmann, C.; Braun, A.; Yoon, W.-S.; Yang, X. Q.; Graule, T. The Fe K-Edge X-Ray Absorption Characteristics of $La_{1-x}Sr_xFeO_{3-\delta}$ Prepared by Solid State Reaction. *Mater. Res. Bull.* **2009**, *44* (6), 1397–1404.

(67) Yang, J. B.; Yelon, W. B.; James, W. J.; Chu, Z.; Kornecki, M.; Xie, Y. X.; Zhou, X. D.; Anderson, H. U.; Joshi, A. G.; Malik, S. K. Crystal Structure, Magnetic Properties, and Mössbauer Studies of $La_{0.6}Sr_{0.4}FeO_{3-\delta}$ Prepared by Quenching in Different Atmospheres. *Phys. Rev. B* **2002**, *66* (18).

(68) Arima, T.; Tokura, Y.; Torrance, J. B. Variation of Optical Gaps in Perovskite-Type 3d Transition-Metal Oxides. *Phys. Rev. B* **1993**, *48* (23), 17006–17009.

(69) Navrotsky, A. Energetics and Crystal Chemical Systematics among Ilmenite, Lithium Niobate, and Perovskite Structures. *Chem. Mater.* **1998**, *10* (10), 2787–2793.

(70) Kawakami, T.; Nasu, S.; Sasaki, T.; Morimoto, S.; Endo, S.; Kawasaki, S.; Takano, M. Charge Disproportionation and Magnetic Order of $CaFeO_3$ under High Pressure up to 65 GPa. *J. Phys. Soc. Jpn.* **2001**, *70* (6), 1491–1494.

(71) Yoo, J. Determination of the Equilibrium Oxygen Non-Stoichiometry and the Electrical Conductivity of $La_{0.5}Sr_{0.5}FeO_{3-x}$. *Solid State Ionics.* **2004**, *175* (1–4), 55–58.

(72) Das, T.; Nicholas, J. D.; Qi, Y. Ionic Conductivity in LSF. *in preparation* **2017**.

(73) Takeda, T.; Yamaguchi, Y.; Watanabe, H. Magnetic Structure of $SrFeO_3$. *J. Phys. Soc. Jpn.* **1972**, *33* (4), 967–969.

(74) Seo, J. W.; Fullerton, E. E.; Nolting, F.; Scholl, A.; Fompeyrine, J.; Locquet, J.-P. Antiferromagnetic $LaFeO_3$ Thin Films and Their Effect on Exchange Bias. *J. Phys. Condens. Matter* **2008**, *20* (26), 264014.

Table 1. Spin-polarized Bader charge analysis of different LSF phases. Magnetic moment calculated by VASP and expected formal charge on Fe are also provided for comparison.

Phase	Bader Analysis						Expected formal charge	Average Fe-O bond length (Å)	VASP magnetic moment (μ_B)	Magnetic moment interpreted charge
	Element	up e	down e	total e	unpaired e	Bader charge (q)				
$LaFeO_3$ (orthorhombic)	La	4.46	4.46	8.92	0.00	2.08+	3.0+	2.046	--	--
	Fe	5.32	0.68	6.00	4.64	2.00+	3.0+		4.23	3.0+
	O	3.74	3.62	7.36	0.12	1.36-	2.0-		--	--
$La_{0.5}Sr_{0.5}FeO_3$ (rhombohedral)	La	4.44	4.43	8.87	0.01	2.13+	3.0+	1.978	--	--
	Sr	4.21	4.21	8.42	0.00	1.58+	2.0+		--	--
	Fe	5.16	0.81	5.97	4.34	2.03+	3.5+		3.94	3.5+
	O	3.68	3.63	7.31	0.05	1.30-	2.0-		--	--
$SrFeO_3$ (cubic)	Sr	4.20	4.19	8.39	0.01	1.60+	2.0+	1.940	--	--
	Fe	4.92	1.04	5.96	3.88	2.04+	4.0+		3.61	4.0+
	O	3.63	3.59	7.22	0.04	1.21-	2.0-		--	--
$SrFeO_2$ (Planar)	Sr	4.22	4.23	8.45	0.01	1.55+	2.0+	2.020	--	--
	Fe	5.24	1.39	6.63	3.86	1.37+	2.0+		3.68	2.0+
	O	3.76	3.69	7.45	0.07	1.46-	2.0-		--	--

Table 2. DFT predictions of stable LSF structures under ground state conditions.

Method GGA + U (=3)		$SrFeO_3$			**LSF55**			$LaFeO_3$		
Input Crystal Structure	**Spin**	**ΔE (eV)**	**μ_B**	**tilt angle**	**ΔE (eV)**	**μ_B**	**tilt angle**	**ΔE (eV)**	**μ_B**	**tilt angle**
Orthorhombic	**FM**	0.00	3.61	177	0.00	3.94	161	0.26	4.23	152
(PNMA)	**AFM**	0.23	3.41	175	0.04	3.76	159	**0.00**	**4.06**	**154**
Rhombohedral	**FM**	0.00	3.61	180	**0.00**	**3.94**	**164**	0.34	4.24	155
(R32)	**AFM**	0.26	3.48	173	0.06	3.78	164	0.05	4.06	157
Cubic	**FM**	**0.00**	**3.61**	**180**	0.09	3.94	180	0.88	4.14	180
(FM-3M)	**AFM**	0.26	3.50	180	0.14	3.74	180	0.40	4.03	180
Experimental (low temp)*		**Helical**[54]	**2.96** [54]	**180** [73]	**FM**[47]	**3.92** [47]	**166** [67]	**AFM**[74]	**4.6±0.2** [49]	**157** [46]

The bold phase data under each column signify the stable structure with the preferred magnetic orientation.

The tilt angle column denotes the average octahedral tilt among Fe-O octahedra in the lattices.

* The last row contains experimental data for comparison.

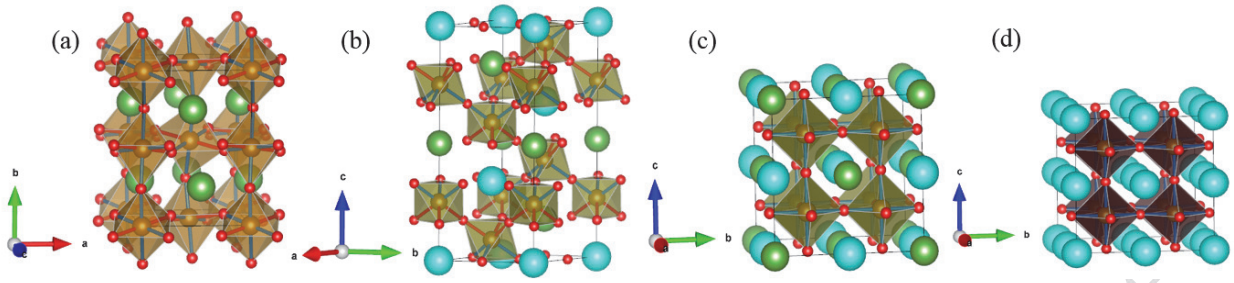

Figure 1. (Color online) DFT calculated lattice structures for (a) orthorhombic $LaFeO_3$, (b) rhombohedral $La_{0.5}Sr_{0.5}FeO_3$, (c) cubic $La_{0.5}Sr_{0.5}FeO_3$, and (d) cubic $SrFeO_3$. Atom colors: La – green, Sr - blue, Fe – brown, O – red. The different Fe-O_6 octahedra colors denote polyhedra with different Fe charge states: Fe^{3+} – light brown, $Fe^{3.5+}$ – moss green, Fe^{4+} – dark brown.

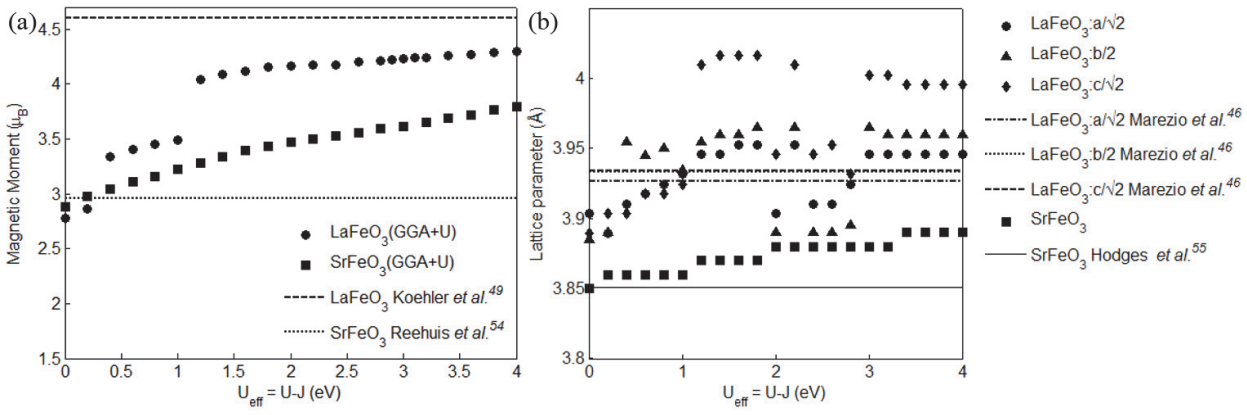

Figure 2. (a) Magnetic moment variation with U for $LaFeO_3$ and $SrFeO_3$. (b) Lattice parameter variation with U for $LaFeO_3$ and $SrFeO_3$. The computational finds (points) in both (a) and (b) are compared with experimental results (dashed horizontal lines).

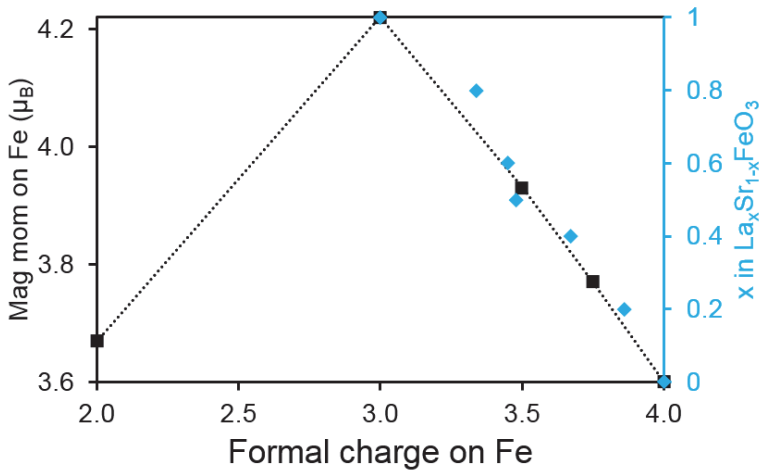

Figure 3. (Color online) Black squares represent the formal charge on Fe resulting from different La/Sr ratios in $La_xSr_{1-x}FeO_3$ calculated from the magnetic moment on Fe with a GGA+U(=3) (left *y*-axis). Blue diamonds show experimentally measuredaverage Fe charge states for varying La/Sr ratios (right *y*-axis). The black dotted line represents the predicted linear relationship between the Fe charge state and the La/Sr ratio.

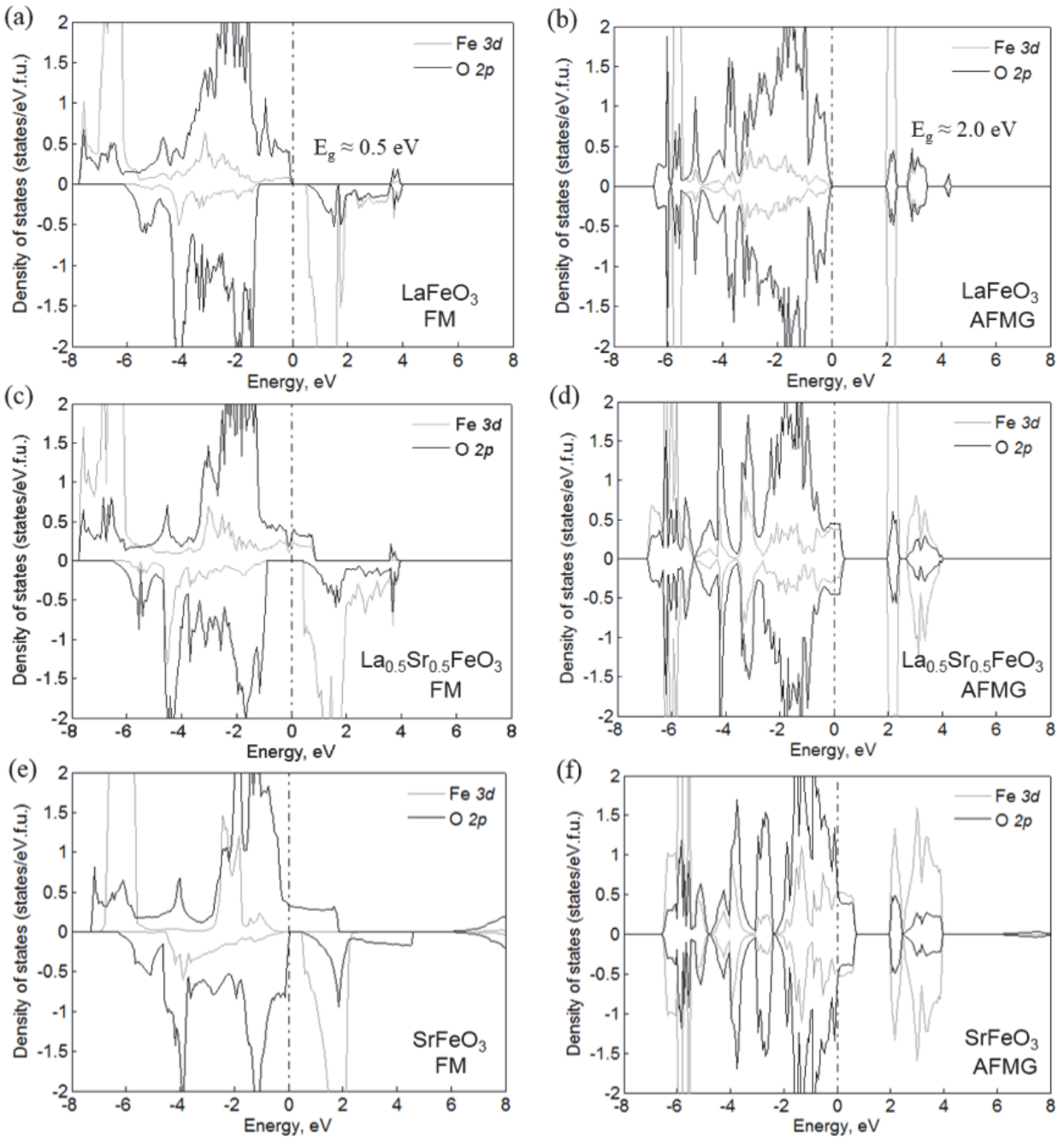

Figure 4. GGA+U (=3) partial density of states calculations for (a-b) orthorhombic $LaFeO_3$, (c-d) rhombohedral $La_{0.5}Sr_{0.5}FeO_3$, and (e-f) cubic $SrFeO_3$. The gray and black lines represent the Fe *3d* and O *2p* states respectively.

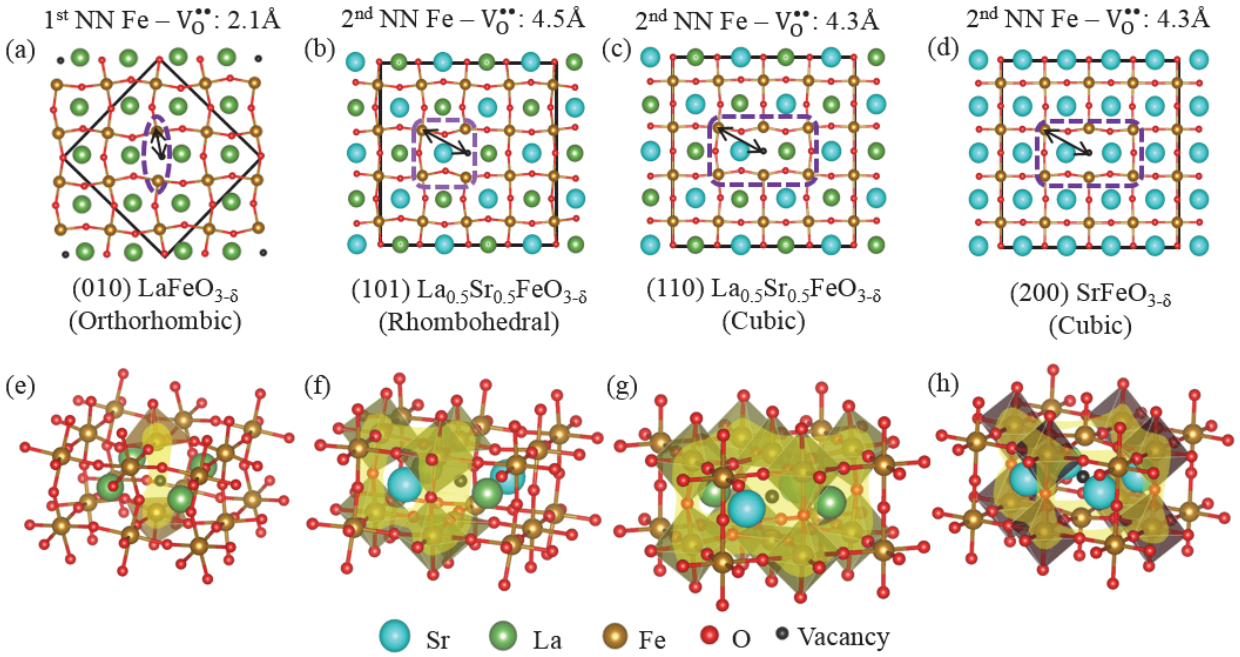

Figure 5. (Color online) Long-range charge transfer areas (denoted by the purple dashed lines in a-d) and perspective views of the $La_xSr_{1-x}FeO_3$ lattice polarons (e-h) for (a, e) orthorhombic $LaFeO_3$, (b,f) rhombohedral $La_{0.5}Sr_{0.5}FeO_3$, (c,g) cubic $La_{0.5}Sr_{0.5}FeO_3$, and (d,h) cubic $SrFeO_3$. Note, in (a-d) different Miller planes were used for each phase to compare lattice orientation with same visual conformity. In (e-h) the polaron shape was highlighting by only drawing sides to those Fe-O polyhedra with an Fe atom that received excess electrons due to oxygen vacancy formation. In (a-d), the black lines indicate the border of the supercells used for computations, while the arrows provide an estimate of the polaron size by denoting the distance the distance from the outermost charge-altered Fe atoms to the oxygen vacancy site.

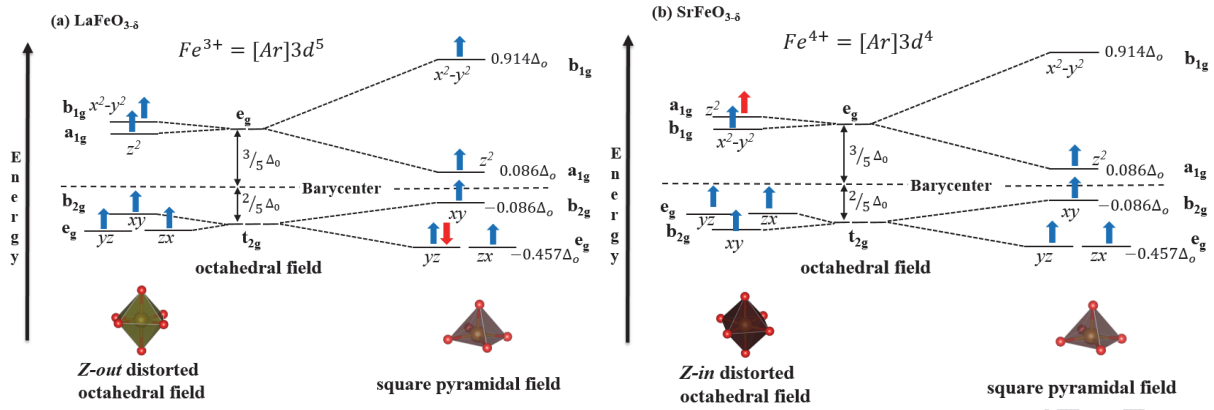

Figure 6. Schematic of the *d*-orbital splitting in the Fe in different polyhedra showing that the excess electrons generated during oxygen vacancy formation (in red) will be localized to oxygen vacancy adjacent square pyramidal Fe in orthorhombic $LaFeO_3$ (a), and transferred to second nearest neighboring octahedral Fe in cubic $SrFeO_3$ (b).

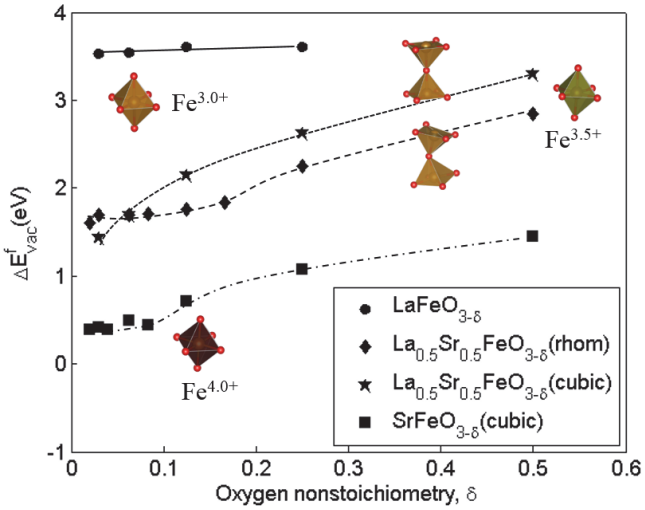

Figure 7. GGA+U calculated oxygen vacancy formation energies for different $La_xSr_{1-x}FeO_3$ compositions. The Fe-O polyhedra represent the charge on Fe in perfect lattice. The lines are guides to the eye.

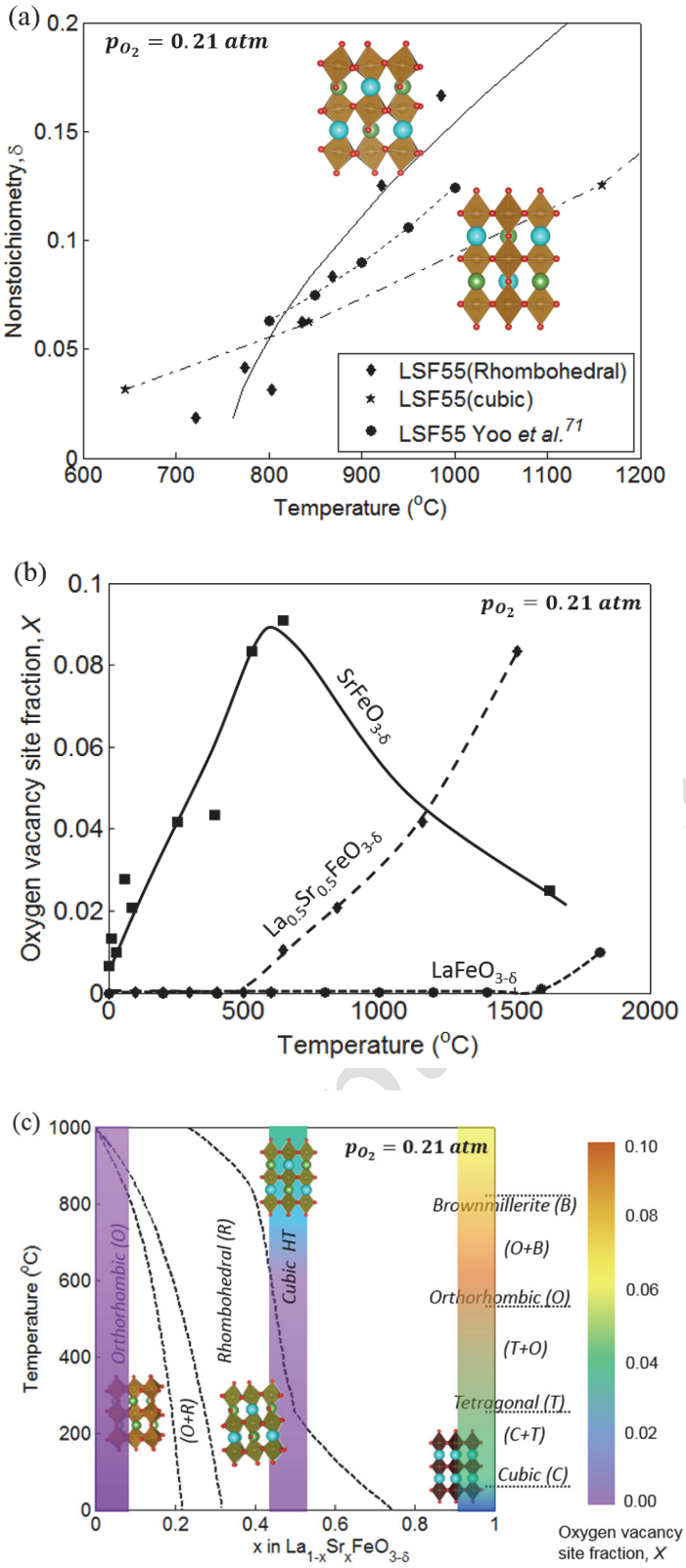

Figure 8. (Color online) (a) The oxygen non-stoichiometry versus temperature in air,(b) the oxygen vacancy site fraction as a function of temperature in air, and (c) the oxygen vacancy site

fraction as a function of temperature and La/Sr ratio for various $La_xSr_{1-x}FeO_3$ phases. Note, the lines in (a-b) and are guides to the eye and the lines in (c) are the experimentally determined phase boundaries.[17,31] The oxygen vacancy site fraction in (c) is denoted by the color overlay and the right-hand color scale. The *X* values in b) and c) are never zero. They are just smaller than can be resolved with the linear *X* scale chosen to highlight the *X* trends discussed here.